The influence of size, shape, and twin boundaries on heat-induced alloying in individual Au@Ag core-shell nanoparticles

The Influence of Size, Shape, and Twin Boundaries on Heat-induced Alloying in Individual Au@Ag Core-Shell Nanoparticles.

Mikhail Mychinko, Alexander Skorikov, Wiebke Albrecht, Ana Sánchez Iglesias, Xiaolu Zhuo, Vished Kumar, Luis M. Liz-Marzán and Sara Bals**

M. Mychinko, A. Skorikov, Dr. W. Albrecht, Prof. Dr. S. Bals
EMAT, University of Antwerp, Groenenborgerlaan 171, 2020 Antwerp, Belgium
E-mail: sara.bals@uantwerpen.be

M. Mychinko, A. Skorikov, Dr. W. Albrecht, Prof. Dr. S. Bals
NANOlab Center of Excellence, University of Antwerp, Groenenborgerlaan 171, 2020 Antwerp, Belgium

Ana Sánchez Iglesias, Dr. Xiaolu Zhuo, Vished Kumar, Prof. Dr. Luis M. Liz-Marzán
CIC biomaGUNE, Basque Research and Technology Alliance (BRTA), Paseo de Miramón 194, 20014 Donostia-San Sebastián, Spain

Ana Sánchez Iglesias, Dr. Xiaolu Zhuo, Prof. Dr. Luis M. Liz-Marzán
CIBER de Bioingeniería, Biomateriales y Nanomedicina (CIBER-BBN), Paseo de Miramón 194, 20014 Donostia-San Sebastián, Spain

Prof. Dr. Luis M. Liz-Marzán
Ikerbasque, Basque Foundation for Science, 48013 Bilbao, Spain

Prof. Dr. Luis M. Liz-Marzán
Department of Applied Chemistry, University of the Basque Country, 20018 Donostia-San Sebastián, Spain

Keywords**:** in situ electron tomography, bimetallic nanoparticles, 3D diffusion simulations, alloying dynamics.

Environmental conditions during real-world application of bimetallic core-shell nanoparticles (NPs) often include the use of elevated temperatures, which are known to cause elemental redistribution, in turn significantly altering the properties of these nanomaterials. Therefore, a thorough understanding of such processes is of great importance. The recently developed combination of fast electron tomography with in situ heating holders is a powerful approach to investigate heat-induced processes at the single NP level, with high spatial resolution in 3 dimensions (3D). In combination with 3D finite-difference diffusion simulations, this method can be used to disclose the influence of various NP parameters on the diffusion dynamics in Au@Ag core-shell systems. A detailed study of the influence of heating on atomic diffusion and alloying for Au@Ag NPs with varying core morphology and

crystallographic details was carried out. Whereas the core shape and aspect ratio of the NPs played a minor role, twin boundaries were found to have a strong influence on the elemental diffusion.

1. Introduction

During the past decades, metal nanoparticles have attracted great attention in material science due to their unique optical properties based on surface plasmon resonances.[1–4] Localized surface plasmons (LSP) correspond to resonant oscillations of conduction electrons produced by interaction with electromagnetic irradiation (e.g. light),[2,5,6] making plasmonic nanoparticles promising candidates for application in sensing,[7,8] photocatalysts,[5] medicine,[9–11] data storage,[12] and solar energy conversion.[13,14] Colloidal synthetic techniques enable scientists to routinely produce mono- and bimetallic nanoparticles (NPs) of various shapes and sizes,[15,16] providing the ability for precise tuning of optical properties.[13, 17-19] Hereby, not only the presence but also the actual distribution of elements within the volume of the particle may govern the properties of nanomaterials.[19–21]

However, the carefully synthesized distribution of elements inside a bimetallic NP might change once the NP is exposed to realistic conditions, such as elevated temperatures, by alloying or interdiffusion.[22,23] The dynamics and mechanism of these processes strongly depend on various aspects, e.g. NP composition,[22,24,25] size[22,26] or shape.[23,27] Additionally, a difference in core-shell interface[27] or the presence of twin boundaries, such as those in pentatwinned NPs, may also play a role.[28,29] Understanding the influence of these parameters is thus of great importance, since alloying can alter the physicochemical and optical properties of bimetallic NPs.[30] On the other hand, precise control over thermal or irradiation conditions may also be beneficial, for instance, leading to dramatically improved monodispersity in Au NPs,[31] superior catalytic performance of Au-Pd alloyed nanospheres,[32] or the development

of novel data storage technologies.[12] In the particular case of Au-Ag nanorods (NRs), alloying has been reported to lead to enhanced chemical stability in harsh environments, preserving excellent LSPR properties in comparison to Au@Ag core@shell structures.[33–35] Despite recent progress concerning the investigation of bimetallic systems using various experimental and simulation techniques, understanding of the mechanisms behind atomic diffusion at the single NP level is still far from complete. In fact, the diffusion dynamics are expected to be different at the nanoscale compared to the bulk, as indicated by orders of magnitude enhanced diffusion coefficients for Au-Ag NPs with sizes smaller than 5 nm, compared to bulk coefficients.[36] Thus, a detailed understanding of nano-alloying processes and their dependence on relevant external stimuli and NP parameters is crucial for further improvement of NP properties and applications.

The recently developed combination of fast tomography based on High-Angle Annular Dark-Field Scanning Transmission Electron Microscopy (HAADF-STEM), together with in situ heating holders, has enabled the investigation of heat-induced processes at the single NP level with high spatial resolution in 3 dimensions (3D).[23,37,38] In this manner, quantification of diffusion coefficients on a single NP level has become possible.[23] Because of its high spatial resolution, fast HAADF-STEM tomography has several advantages in comparison to ensemble-based techniques, such as Vis-IR spectroscopy[39] or extended X-ray absorption fine structure (EXAFS).[40] Since electron tomography enables the investigation in 3D (over the volume of the NP), this approach is also superior to conventional two-dimensional (2D) (S)TEM techniques.[22,36] Major drawbacks of the techniques mentioned above, such as averaging of data over a large number of particles or the inability of performing in situ investigations in 3D, may result in discrepancies between different studies, especially for objects with complex morphologies. For example, significant divergence in alloying

temperatures[22,33] or disagreement in diffusion speeds[22,23,26] for Au@Ag NPs of similar compositions and sizes have been reported.

In this study, we used fast HAADF-STEM to perform 3D in situ investigations of different NPs under heating at 450 °C. We focused on single-crystalline and pentatwinned Au@Ag core-shell NPs with different sizes, aspect ratios and overall shapes. By characterizing NPs with a different core morphology, the effect of the type of interfacial facets could also be investigated. A careful comparison enabled us to study the influence of each isolated factor on the alloying kinetics. For all of these systems, the diffusion dynamics was quantified by comparing experimental data to finite difference diffusion simulations based on Fick's law. Our experiments yield novel insights on how parameters such as size, aspect ratio, core shape and the presence of twin boundaries influence heat-induced alloying in bimetallic core-shell NPs. We envision that the acquired knowledge will be of great importance to improve the use of bimetallic NPs in real applications.

2. Results and discussion

Samples characterization and experimental conditions

Au-Ag NPs are ideal for the investigation of interdiffusion dynamics, since Au and Ag both crystallize in the *fcc* crystal lattice with almost identical lattice constants (0.408 nm for Au and 0.409 nm for Ag). This makes the elements completely intermixable, without significant lattice strain, and allows them to form alloys in the whole range of concentrations. Moreover, Au@Ag NPs are relatively stable under beam exposure in a TEM, while the significant difference in atomic number Z enables one to reveal Au and Ag distributions using HAADF-STEM. In our previous work, we implemented a fast HAADF-STEM tomography approach, which allowed us to perform a quantitative analysis of the elemental redistribution in 3D for Au@Ag core-shell nanorods and nanotriangles.[23] Although these experiments

served as a proof of principle of the technique, detailed understanding of key influences in the elemental redistribution process of nanomaterials is still lacking. Here, we extended the analysis of elemental redistribution in Au@Ag NPs to investigate the effects of size, aspect ratio, overall morphology, shape of the core and the presence of twin boundaries. We focused on Au@Ag NPs with the following morphologies: single-crystalline (SC) Ag nanocubes (NC) with either octahedral (OCT) or spherical (SP) Au cores, SC Ag nanorods (NRs) with Au NR cores and pentatwinned (PT) Ag NRs with NR or bipyramid (BP) Au cores. An overview of the investigated systems is provided in **Table 1**, where we also included representative 3D visualizations of the corresponding tomography reconstructions for all NP types in their initial (room temperature) state.

It should be noted that, thermodynamically driven reshaping of anisotropic morphologies due to atomic redistribution at the NP surface may hinder the interpretation of alloying experiments and even alter the mechanism of elemental redistribution.[27,37,41,42] Moreover, because of the lower activation energies, surface diffusion is typically faster in comparison to volume diffusion. To minimize reshaping of the NPs upon heating, all particles studied in this work were coated by a 20 nm thick mesoporous silica-shell (m-SiO_2).[43]

Table 1. Selected parameters of the investigated Au@Ag@m-SiO_2 NPs. We use the following abbreviations to describe the different types of NPs: SC – single-crystalline, PT – pentatwinned, NC – nanocube, NR – nanorod, BP – bipyramid, OCT – octahedron, SP – sphere. Volumes and AR values were extracted from 3D reconstructions of the initial (RT) state for all presented Au@Ag NPs, excluding the m-SiO_2 shell. Scale bars correspond to 20 nm.

NPs	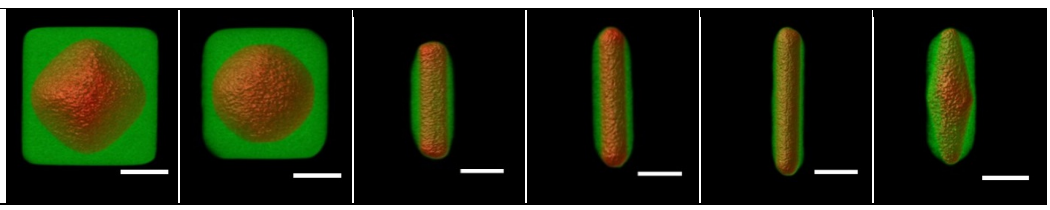

	NC1	NC2	NR1	NR2	NR3	NR4
Au core	SC-OCT	SC-SP	SC-NR	SC-NR	PT-NR	PT-BP
Ag shell	SC-NC	SC-NC	SC-NR	SC-NR	PT-NR	PT-NR
Volume [10^3 nm^3]	195	148	14.1	24.7	17.5	27.5
AR	1	1	2.3	3.7	4.1	3.1
Au : Ag [at. %]	22 : 78	24 : 76	43 : 57	46 : 54	43 : 57	44 : 56

Prior to the actual alloying experiments, we carefully determined the most suitable experimental conditions to be used during in situ investigations. For example, reported alloying temperatures for Au@Ag core-shell NPs with sizes comparable to those used in this paper range between 350 and 450 °C.[22,33] In order to determine an optimal alloying temperature, a preliminary in situ experiment was carried out. Relevant particles were hereby deposited from a colloidal dispersion on a microelectromechanical system (MEMS)-based heating chip and heated in situ from 20 up to 500 °C, in steps of 50 °C. The NPs were kept at the selected temperature for 5 minutes and the system was subsequently cooled down to room temperature. 2D HAADF-STEM images were acquired after every heating step for an overall visualization of the elemental redistribution and potential reshaping. A slight reshaping, possibly due to a certain degree of flexibility of the mesoporous silica shell, was indeed observed around the tip of Au@Ag NRs at 250 °C, as marked by white arrows in **Figure S1** in the Supporting Information. However, the overall shape of the NRs was preserved, even at longer heating steps and higher temperatures. From **Figure S1** it is furthermore clear that alloying started to occur within the temperature range of 300-350 °C. For all subsequent experiments, we selected an operating temperature of 450 °C, which provided optimal alloying kinetics to track the most pronounced elemental redistribution during the first heating steps, while ensuring complete alloying within a time period of a few minutes.

In situ 3D investigation of heat-induced metal redistribution in individual Au@Ag core-shell NPs was performed by HAADF-STEM tomography using a DENSsolutions Wildfire MEMS-based heating sample holder, optimized for electron tomography. To induce alloying, all particles were heated at 450 °C for a total of 600 seconds. Energy-Dispersive X-ray Spectroscopy (EDX) mapping was performed for each particle before (0 seconds) and after heating (600 seconds) to confirm complete and uniform alloying at the final stage (**Figures S2**, **S3a-d** in the Supporting Information). To investigate intermediate states, the heating process was interrupted after 15, 30, 45, 60, 90, 120, 180, 300 and 600 seconds by fast cooling (within less than 1 second), down to room temperature. After every heating interval, a fast tilt series for tomography was acquired. From the 3D reconstructions, retrieved from every tilt series, we calculated the volumes of the investigated NPs. In this manner, we confirmed that the volume did not change for any of the studied NPs during heating. An example for NC2 is shown in **Figure S3e**. Given that both the volume and composition of all investigated NPs remained constant, we assume that both Au and Ag redistributed only at the surface and within the volume of the presented NPs.

Alloying of Au@Ag single-crystalline nanocubes

We first applied our method to NCs with different shapes for the core: a slightly truncated octahedron for NC1 and a sphere for NC2 (**Figure 1a** and **Table 1**). The Au octahedral core for particles such as NC1 is mostly confined by (111) facets, whereas the Au sphere surface is formed by a wide variety of higher order facets.[44] In both NC1 and NC2, the Au cores were encapsulated by an Ag cube. By comparing the different types of NC, we can obtain a comprehensive understanding of diffusion processes across different interfacial planes and along different axes in a single-crystalline structure.

Figures 1b and **1c** illustrate the outcome of our experiments by showing slices through the 3D HAADF-STEM reconstructions along the [100] and [110] zone axes. Since the intensity in HAADF-STEM images scales with the atomic number Z of the elements that are present, our 3D reconstructions could be translated into compositions by using a quantitative methodology as outlined in the Methods section and explained in our previous work.[23] From the slices in **Figures 1b** and **1c**, the redistribution of Au and Ag along different directions and after every heating interval at 450 °C can be readily monitored. It can be seen that alloying proceeds uniformly in all directions. These findings are in good agreement with existing literature, where it has been reported that the extent and frequency of atomic exchange events are expected to be the same for all directions in close-packed structures, as is the case for the *fcc* crystalline cell of both Au and Ag.[45]

However, we notice a faster alloying rate for NC2 (**Figure 1c**) as compared to NC1 (**Figure 1b**), which may be related to the slightly smaller volume of NC2 (**Table 1**) and therefore, shorter distances for atoms to diffuse until alloying is completed. It is important to note that, on the basis on this qualitative comparison only, it is impossible to determine if the volume or the different morphology of the core and therefore different interfacial facets are responsible for the differences in the alloying behavior.

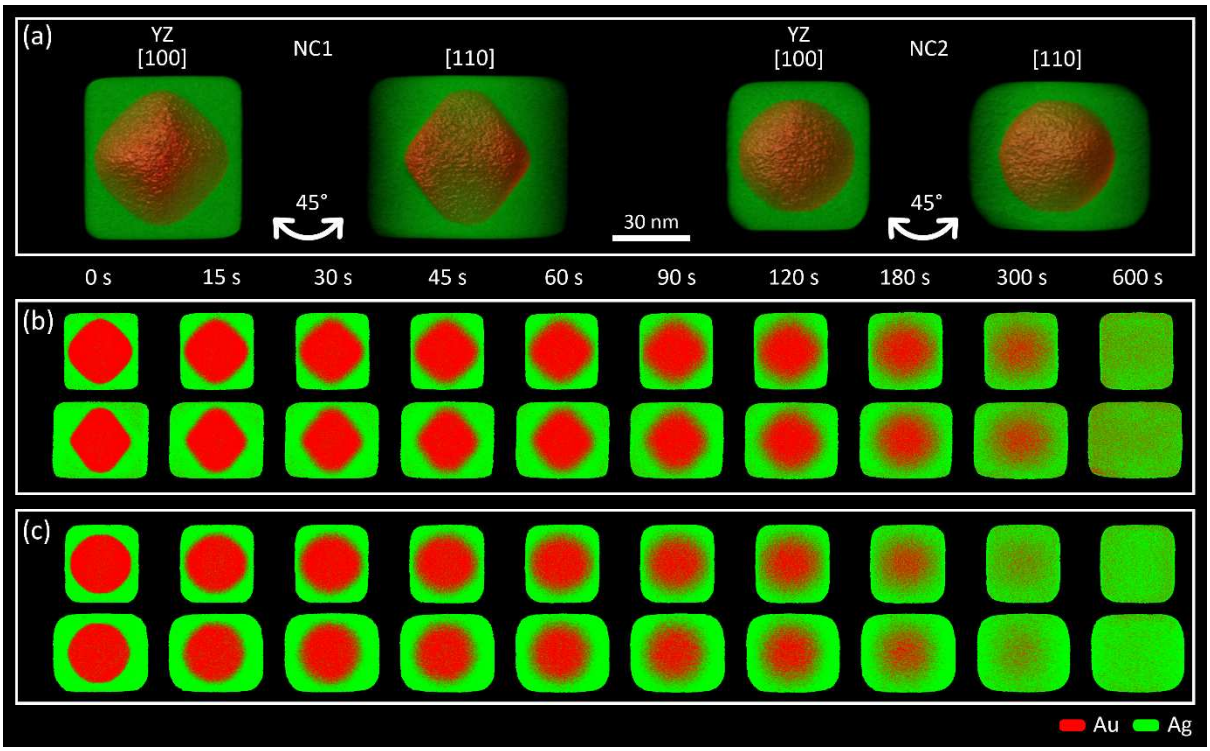

Figure 1. (a) Visualization of 3D reconstructions for NC1 and NC2, presented along [100] and [110] directions. (b,c) Corresponding slices through the 3D reconstructions, yielding the elemental distributions in NC1 (b) and NC2 (c), at different stages during alloying at 450 °C.

Based on the 3D reconstructions, we could quantify the degree of alloying after each heating interval (**Figure 2a**). The quantification procedure is based on the spread in the voxel intensity histogram and detailed in the Methods section.[23] Hereby, the point of 100% alloying is defined by simulating the fully alloyed particle, adding experimental noise and including missing wedge artifacts. The latter occur due to the limited tilting range of the heating tomography holder (±70°), resulting in the absence of data along a certain angular range during reconstruction. These artifacts may yield pixels with lower intensity along the missing angles direction, which in our case will be misinterpreted as Ag atoms. After taking these effects into account, we determined alloying degrees of 92% and 96% after heating to 450 °C for 600 seconds, for NC1 and NC2, respectively. Not surprisingly, these small differences could not be identified by 2D EDX maps (**Figure S3**, Supporting Information), which showed an apparently uniform distribution of Au and Ag inside the nanocrystals. In agreement with the visual

interpretation from **Figure 1**, **Figure 2a** confirmed the slightly slower alloying of NC1 compared to NC2.

In order to eliminate the influence of NC volume and to enable a direct comparison between NC1 and NC2, we performed 3D diffusion simulations based on a finite-difference approximation of Fick's law using the tomography reconstruction at room temperature for each particle as an input (see Methods section for details).[23] During our experiments, we observed that both particles underwent minor reshaping during heating, leading to slightly more rounded vertices and edges, which should be considered for a more accurate quantitative description.[23] Hence, the observed reshaping was included in our simulations by applying a mask, corresponding to the deformed shell of the NP, to the reconstruction obtained at room temperature. The resulting morphology was then used as an input for diffusion simulations. Moreover, missing wedge artifacts together with Poisson noise were also included in the simulations to make a more accurate comparison with the experimental results. By fitting the outcome of the simulations using different diffusion coefficients to our experimental observations (see Methods section for details), we were able to determine the best match for this coefficient, as shown in **Figures 2b** and **2c**. The optimal fit corresponds to the blue dashed lines with diffusion coefficients of $(2.7 \pm 0.1)\times10^{-19}$ m^2s^{-1} for NC1 and $(2.4 \pm 0.2)\times10^{-19}$ m^2s^{-1} for NC2. **Figures 2d** and **2e** show slices through the experimental 3D reconstructions and the corresponding simulations along the [100] direction. We thus conclude that the diffusion coefficients for NC1 and NC2, which are not influenced by differences in NC volume, have comparable values. These results therefore indicate that the interdiffusion kinetics at high temperature in isotropic single-crystalline Au@Ag NPs do not appreciably depend on the details of the Au-Ag interface.

Figure 1 shows that the time for complete alloying for NC1 is slightly longer in comparison to NC2, whereas both NCs have similar values for the diffusion coefficient.

Whereas this observation may appear as counterintuitive, diffusion in larger particles requires a longer diffusion time, since atoms need to redistribute over longer distances. In a smaller particle (with similar composition and morphology), diffusion is expected to take a shorter time, provided that the diffusion coefficients values are equal for both particles. To illustrate the effect of particle size on alloying time, we simulated alloying for three NCs with the same morphology and composition (based on NC1), but with different sizes: cubes with edge lengths of 60, 45 and 75 nm. The diffusion coefficient for these three cases was found to be equal to the value obtained for NC1 (2.7×10^{-19} m^2s^{-1}). As can be seen from **Figure S4**, the complete alloying time noticeably increases with a corresponding increase in particle volume. These observations illustrate the difference between alloying time, which depends on particle volume, and diffusion coefficient, which is independent on particle volume. In order to estimate the effects of other parameters (morphology, composition, presence of defects), it is therefore important to compare diffusion coefficients.

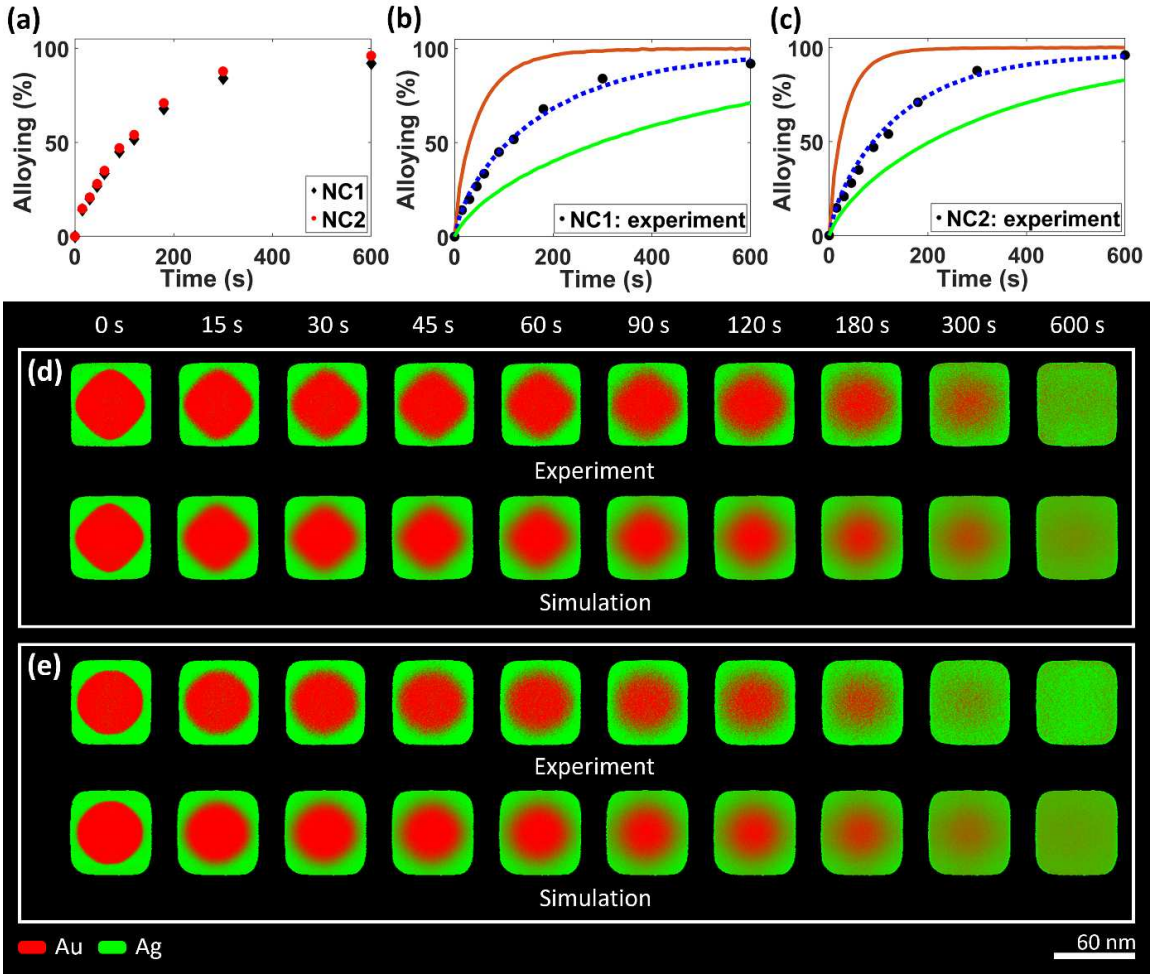

Figure 2. (a) Comparison of the alloying progress for NC1 and NC2. (b,c) Comparison of the experimental results to the diffusion simulations performed for different diffusion coefficients. The degree of alloying was quantified from the experimental data (black circles) for NC1 and NC2, respectively. The blue dashed curves correspond to the best fit of simulations to the experiments for diffusion coefficients of 2.7×10^{-19} m^2s^{-1} for NC1 (b) and 2.4×10^{-19} m^2s^{-1} for NC2 (c). For both NCs, the red curves correspond to simulations based on a diffusion coefficient of 10×10^{-19} m^2s^{-1}, whereas the green curves were obtained using a diffusion coefficient of 1.0×10^{-19} m^2s^{-1}. (d,e) The upper rows show slices through the experimentally determined 3D elemental distribution in NC1 and NC2, respectively, at different stages of alloying. The lower rows display slices through the simulated 3D elemental distributions using the optimal diffusion coefficient.

Alloying of Au@Ag single-crystalline and pentatwinned nanorods

To investigate the effect of aspect ratio, presence of twin boundaries and core shape during heat-induced alloying, four different types of Au@Ag NRs with similar compositions were studied (**Table 1**: NR1-4 and **Figure 3a**). For comparison, we selected pairs of NRs, which differ in only one parameter: aspect ratio in the case of NR1 and NR2, absence or presence of twin planes and a different shape of the core for NR2 and NR3. Finally, we also compared NR3 and NR4, both PT-NRs, but with a PT-NR and a PT-BP core, respectively. For each comparison, the other parameters had similar values, which enabled us to investigate the separate influence of each factor on the alloying dynamics. Any dependence on volume could again be eliminated by comparing the extracted diffusion coefficients.

Figure 3b,c shows the experimental results for all four NRs. Similar to the NCs, elemental diffusion proceeded uniformly in all directions. It should be noted that the influence of the missing wedge was clearly visible on the orthoslices in the XY-direction, manifesting itself as apparent Ag-rich regions along the vertical direction. This emphasizes the importance of including the missing wedge artifact in the diffusion simulation for accurate retrieval of the diffusion coefficients. In addition, for the larger PT-BPs (NR4) a darker and hence seemingly greener region in the YZ orthoslices in the middle of the particle could be observed. We attribute this effect to remaining diffraction contrast due to the pentatwinned structure.

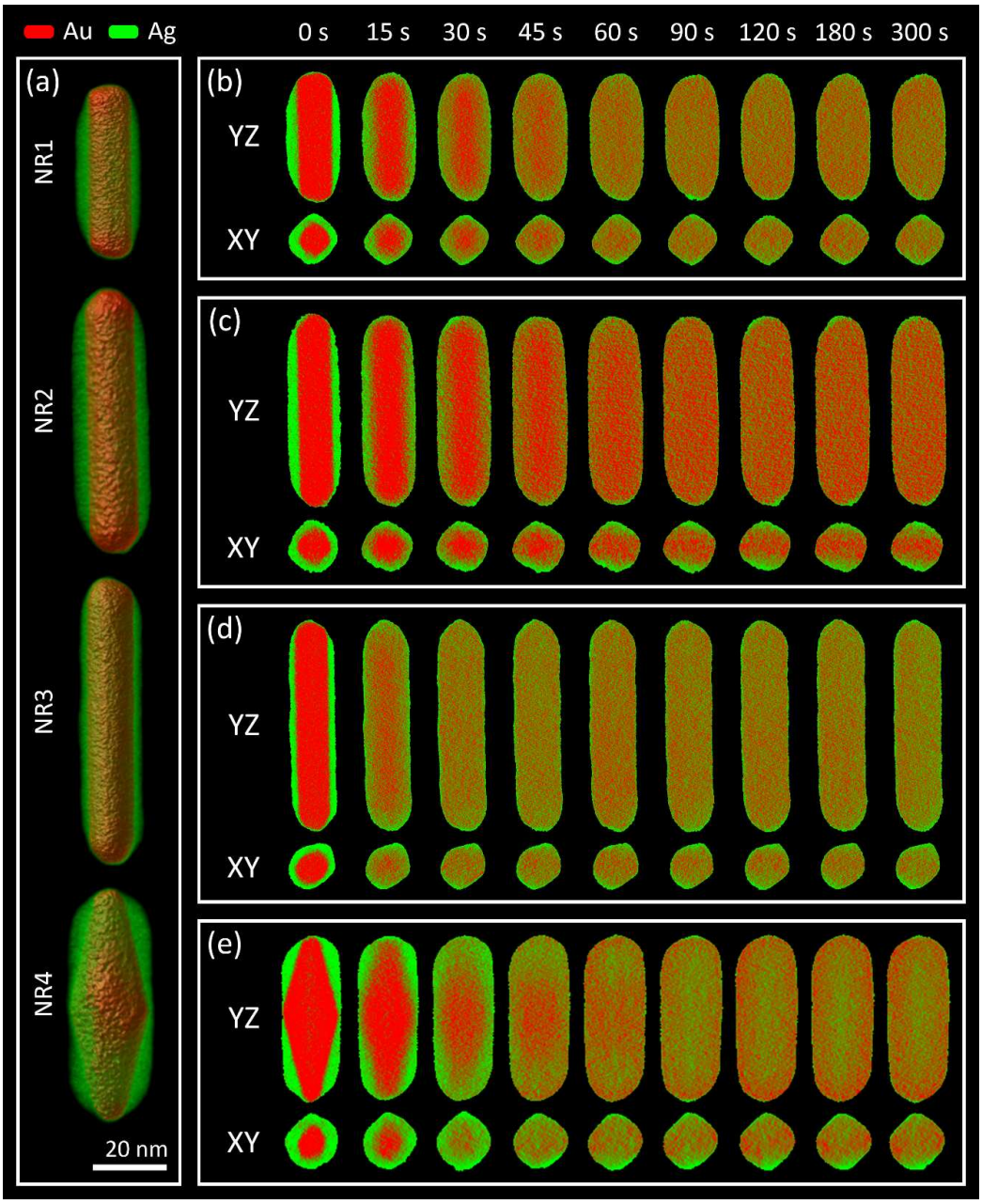

Figure 3. (a) Visualization of 3D reconstructions for NR1, NR2, NR3, and NR4. (b-e) YZ- and XY- slices through the 3D reconstructions of elemental distributions at different stages of alloying at 450 °C.

The degrees of alloying for all NRs were calculated from 3D reconstructions after each heating interval, in the same manner as described above for NCs, and the results are presented in **Figure 4a**. The best fits of the 3D diffusion simulations to the experimental data are summarized in **Figure 4b-e**. An enlarged part of **Figure 4d** is shown in **Figure S5** (Supporting

Information) to show the differences between simulated curves and experimental data in more detail. The corresponding fitted diffusion coefficients are listed in **Table 2**, together with values for NC1 and NC2, as a reference. YZ-slices through the 3D simulated reconstructions after each heating step, as well as the corresponding experimental YZ-slices, are presented in **Figure 4f-i** for all NRs. Also for NRs, fitting of the simulated diffusion curves resulted in good agreement with the experimental data, confirming the appropriate performance of our simulation model, which results in reliable diffusion coefficients. However, a slight difference in apparent composition between simulations and experimental results could be observed during the latter heating steps (**Figure 4f-i**). This cannot be related to actual differences in composition, which are the same for the experiments and simulations and stayed constant over the course of the experiment.

Table 2. Table 2. Values for diffusion coefficients, obtained by 3D diffusion simulations and comparison to experimental data. Uncertainties for the diffusion coefficients were estimated by fitting the experimental data with simulated alloying curves and correspond to the standard deviation of this parameter.

Particle	Defect structure	Core-Shell morphology	Volume [10^3 nm^3]	AR	Au : Ag [at.%]	D [10^{-19} m^{2}s^{-1}]
NC1	SC	OCT @ NC	195	1	22 : 78	2.7 ± 0.2
NC2	SC	SP @ NC	148	1	24 : 76	2.4 ± 0.3
NR1	SC	NR @ NR	14.1	2.3	43 : 57	3.4 ± 0.4
NR2	SC	NR @ NR	24.7	3.7	46 : 54	2.9 ± 0.2
NR3	PT	NR @ NR	17.5	4.1	43 : 57	6.0 ± 0.2
NR4	PT	NBP @ NR	27.5	3.1	44 : 56	6.3 ± 0.4

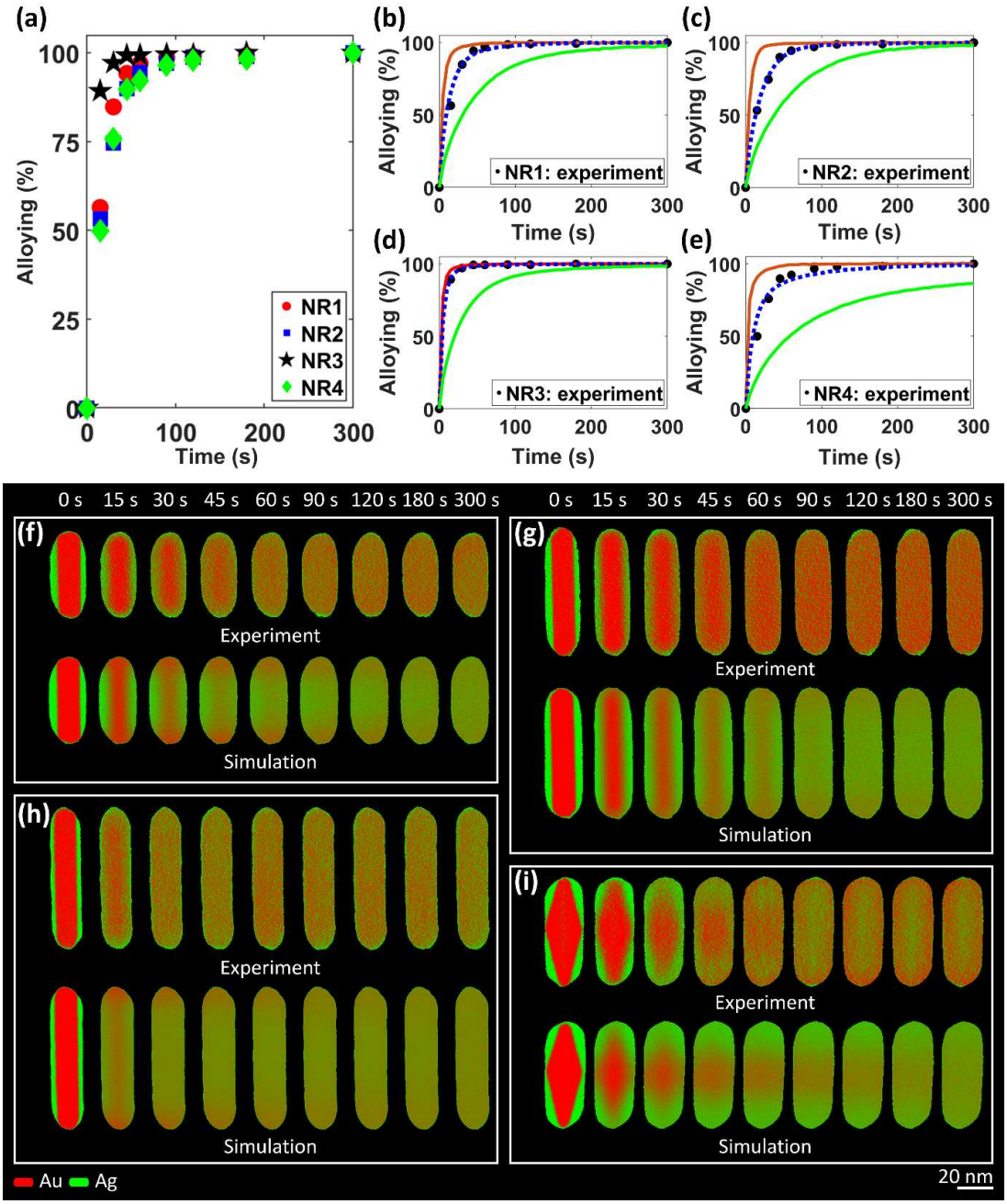

Figure 4. (a) Comparison of the alloying progress for NR1-4; (b–e) Comparison of the experimental results and diffusion simulations performed for different diffusion coefficients. The degree of alloying was quantified from the corresponding experimental data (black circles) for NR1-4. The blue dashed curves correspond to the best fit of simulations to experiments for diffusion coefficients of 3.4×10^{-19} m^2s^{-1} (b), 2.9×10^{-19} m^2s^{-1} (c), 6.0×10^{-19} m^2s^{-1} (d), and 6.3×10^{-19} m^2s^{-1} (e), for NR1-4 respectively. For all NRs, the red curves correspond to simulations based on a diffusion coefficient of 10×10^{-19} m^2s^{-1}, whereas the green curves were obtained

using a diffusion coefficient of 1.0×10^{-19} m^2s^{-1}; (f–i) The upper rows display slices through the experimentally determined 3D elemental distribution for the various NRs at different stages of alloying. The lower rows display slices through the simulated 3D elemental distribution using the optimal diffusion coefficients.

From **Table 2**, we conclude that the obtained values of diffusion coefficients for all NPs investigated in this work are of the same order of magnitude as those reported for Au and Ag interdiffusion in bulk Au-Ag solid solutions and for single-crystalline Au/Ag thin films.[46,47] This suggests that the difference in the volumes of the NPs at the investigated length scale does not affect the alloying dynamics significantly. A slightly higher diffusion coefficient can be observed for SC-NRs when compared to SC-NCs. In this case, the difference in composition (~45 at.% of Au for NR1 and NR2, ~23 at.% of Au for NC1 and NC2) plays a role in the alloying dynamics, due to the different mobility of Ag and Au atoms. Indeed, for particles with a higher Ag content, relatively slow Au atoms limit the alloying rate, since they require longer times to diffuse over longer distances and to get uniformly redistributed within the volume of the particle. A composition-dependent behavior of alloying in Au@Ag NPs of comparable sizes has been reported elsewhere.[22,23]

Interestingly, about twice higher diffusion coefficients were obtained for PT-NRs (6.0×10^{-19} m^2s^{-1} for NR3 and 6.3×10^{-19} m^2s^{-1} for NR4) in comparison to SC-NRs (3.4×10^{-19} m^2s^{-1} for NR1 and 2.9×10^{-19} m^2s^{-1} for NR2). The faster diffusion observed for PT-NRs can likely be attributed to a faster atomic transport due to distortions in the crystal lattice, caused by defects. The boundary between two twin planes may contain a higher amount of vacant sites and longer distances between neighboring sites, thereby creating pathways for faster and easier atomic transport along these boundaries. A similar enhancement of diffusion kinetics due to the presence of twin boundaries has been previously suggested in the literature,[48] whereas the presence of lattice vacancies was shown to significantly increase diffusion dynamics in

bimetallic NPs.[26,45] As an additional proof of the faster diffusion in the presence of twin boundaries, it should be noted from **Figure S1** (Supporting Information) that the starting alloying temperature for PT-NRs (~300 °C) is lower than that for SC-NRs of comparable volume (~350 °C).

Based on the comparable values of the diffusion coefficients for NR1 and NR2, we can conclude that a difference in AR (2.3 vs. 3.7) in rod-like Au@Ag NPs did not affect the diffusion dynamics significantly. Along with the difference in AR, NR3 (AR=4.1) and NR4 (AR=3.1) also displayed a different morphology for the Au core (PT-NR and PT-BP), leading to different interfacial facets. Still, these NRs yielded comparable diffusion coefficients. Together with the results obtained for NC1 and NC2, this allows us to conclude that the kinetics of alloying in isotropic and anisotropic Au@Ag NPs do neither depend on the direction of diffusion inside the lattice cell nor on the difference in the type of Au-Ag interfacial facets. Interestingly, these findings are not in agreement with the alloying behavior reported for Pd@Pt NPs, where a lower temperature threshold for core-shell interdiffusion was observed for octahedral core-shell NPs in comparison to cubic core-shell NPs. [27] This was explained by a higher tendency for subsurface Pt vacancy formation in octahedra than in cubes, which governs interdiffusion of atoms between core and shell of the NP.[27] Enhanced diffusion kinetics in the presence of vacancies in the vicinity of the bimetallic interface was observed for Au@Ag NPs.[26] However, these investigations were performed for spherical NPs, where no information about the influence of Au-Ag boundary faceting could be extracted.

Since all NP systems described so far yielded diffusion coefficients comparable to the bulk scale, we investigated an even smaller nanorod (SR), with aspect ratio and composition similar to NR1, but with significantly (~10 times) smaller volume (**Figure S6a**, Supporting Information). From a visual inspection, the SR appeared to be fully alloyed after a short heating time between 5 and 10 seconds. Despite the presence of a mesoporous-silica shell and shorter

heating times, we observed a significant reshaping of the SR, meaning that at this scale surface diffusion, or even local melting, dominated over lattice diffusion. The main reason for the lower stability of the SRs is the significantly higher fraction of active and mobile surface Ag atoms, which can be estimated from the surface-to-volume ratio of these NPs: 0.49 nm^{-1} for the SR vs. 0.26 nm^{-1} for NR1. Still, we can approximately estimate the value of the diffusion coefficient for the selected SR, by performing 3D simulations of elemental diffusion, using the initial shape and elemental distribution from experimental data in the same manner as explained above. As can be seen from the simulations for different diffusion coefficients in **Figure S7** (Supporting Information), the SR would be fully alloyed after 5 seconds if $D = 10\times10^{-19}$ m^2s^{-1}. For simulations performed using $D = 1\times10^{-19}$ m^2s^{-1}, incomplete alloying was obtained after 10 seconds. Since the experimental data (**Figure S6c**) show that the SR was not completely alloyed after 5 seconds of heating at 450 °C, we can assume that the value of the diffusion coefficient for this SR is within the same order of magnitude as those obtained for the larger NRs (between 1×10^{-19} m^2s^{-1} and 10×10^{-19} m^2s^{-1}). In the literature, very fast diffusion rates ($D \sim 10^{-14}$ m^2s^{-1}) have been reported for 5 nm Au@Ag spherical NPs at even lower temperatures.[36] Therefore, we could expect that below a certain NP volume, alloying dynamics drastically increase possibly due to size confinement effects, e.g. higher ratio of mobile surface atoms. However, these observations were made from images in 2D rather than in 3D. Therefore, a more accurate evaluation of the diffusion dynamics in 3D is important to gain a more detailed understanding of the nature of alloying for such small NRs. However, for this to be achieved with our current method, more elaborate simulations of surface diffusion or alternative synthetic techniques are needed, which would prevent interfering surface diffusion, for example, by encapsulation of NPs with a more rigid shell, e.g. a thin amorphous carbon layer.[39,49]

3. Conclusion

By combining fast electron tomography with an *in situ* heating holder and elemental diffusion simulations, we quantitatively investigated the influence of size, aspect ratio, core morphology and the presence of twin boundaries on the dynamics of alloying of Au@Ag core-shell NPs in 3D. We observed that the diffusion dynamics did not depend on the crystallographic direction and type of interfacial facets between Au and Ag in an *fcc* lattice. On the other hand, we obtained evidence showing that the presence of twin boundaries significantly increased the value of the atomic diffusion coefficient, presumably due to the formation of distortions and vacant sites in the crystal lattice, facilitating the diffusion of atoms. In contrast, the specific details of interfacial crystal planes did not appear to make a big difference in the diffusion coefficient. We also conclude that the values of the obtained diffusion coefficients are in the same range as tabulated values for bulk materials, which indicates a minor influence of particle volume on the alloying kinetics of NPs. Finally, we observed that for small nanorods, with a diameter of 10 nm, surface effects dominated over elemental diffusion.

4. Methods

Chemicals: Gold (III) chloride trihydrate ($HAuCl_4 \cdot 3H_2O$, ≥ 99%), citric acid (≥ 99.5%), sodium borohydride ($NaBH_4$, 99%), L-ascorbic acid (AA, ≥ 99%), silver nitrate ($AgNO_3$, ≥ 99%), 1-decanol (*n*-decanol, 98%), tetraethyl orthosilicate (TEOS, 98%), sodium hydroxide (NaOH, 97%), benzyldimethylhexadecylammonium chloride (BDAC), 3-butenoic acid (97%), hexadecyltrimethylammonium bromide (CTAB, ≥ 99%) and hexadecyltrimethylammonium chloride (CTAC, 25 wt% in water) were purchased from Sigma-Aldrich. Hydrochloric acid solution (HCl, 37 wt%) and ethanol (99.5 %) were purchased from Scharlau. All chemicals were used without further purification. Milli-Q water (resistivity 18.2 MΩ·cm at 25 °C) was

used in all experiments. All glassware was cleaned with aqua regia, rinsed with Milli-Q water, and dried before use.

Synthesis of single crystalline Au octahedra:[44] Gold octahedra were synthesized by reducing $HAuCl_4$ on preformed single crystalline gold nanorods, using butenoic acid as reducing agent. The as-prepared SC AuNRs (experimental details below, length: 41 ± 1 nm, width: 11 ± 2 nm) were purified twice by centrifugation (8500 rpm, 25 min) to remove excess reactants. The purified SC AuNRs were redispersed in an aqueous CTAB solution (10 mM) to a final gold concentration of 6 mM. In a typical synthesis, $HAuCl_4$ (0.1 mL, 50 mM) was mixed with an aqueous CTAB solution (10 mL, 10 mM) and then an aliquot of concentrated butenoic acid (0.04 mL) was added into the mixture to reduce partially the gold salt from Au^{3+} to Au^{+}. The reaction mixture was kept at 60 °C and the color of the solution changed gradually from light yellow to colorless, indicating Au^{3+} reduction. Subsequently, a certain volume of purified SC AuNRs (0.08 mL, 6 mM) was added to the mixture under vigorous stirring and the reaction vessel was kept at 60 °C for 5 h to ensure completion of Au octahedra growth. The final lateral dimension of gold octahedra was 46 ± 1 nm. As prepared Au octahedra were washed twice with an aqueous BDAC solution (10 mM) by centrifugation (5000 rpm, 30 min) and redispersion of the precipitate in BDAC (10 mM), to a final gold concentration of 0.25 mM.

Synthesis of single crystalline Au nanospheres (SC AuNSs):[50] Single crystalline gold nanospheres were synthesized via successive seed-mediated growth. First, gold seeds (~1.5 nm) were prepared by sodium borohydride (0.3 mL, 10 mM) reduction of $HAuCl_4$ (0.25 mM, 5 mL) in aqueous CTAB solution (100 mM). After 30 min, an aliquot of seed solution (0.6 mL) was added to a growth solution (100 mL) containing CTAC (100 mM), $HAuCl_4$ (0.18 mM), and AA (0.36 mM). The mixture was left undisturbed for 2 h at 25 ºC. Upon synthesis, the solution containing 10 nm gold nanospheres was centrifuged (9000 rpm, 2 h) to remove excess CTAC and ascorbic acid, and redispersed in an aqueous BDAC solution (10 mM) to a final gold

concentration equal to 2.5 mM. To grow 10 nm gold nanospheres up to 40 nm, the seed solution (0.08 mL, 2.5 mM) was added under vigorous stirring to a growth solution (25 mL) containing BDAC (100 mM), $HAuCl_4$ (0.5 mM), and AA (1 mM). The mixture was left undisturbed for 30 min at 30 ºC, and then washed twice by centrifugation. The particles were finally dispersed in BDAC (10 mM) to a final gold concentration of 0.25 mM. The final diameter of SC AuNSs was 38 ± 1 nm.

Synthesis of single crystalline Au nanorods (SC Au NRs):[51] Au NRs were prepared using a modified seed-mediated approach. First, two separate CTAB/n-decanol stock solutions were prepared by separately adding 1.068 g (13.5 mM) and 870.5 mg (11 mM) of n-decanol in two different 500 mL Erlenmeyer flasks, each containing 9.111 g of CTAB (50 mM). 500 mL of Milli-Q water was then added to each flask and the obtained mixtures were stirred for 3-4 hours at 35 ºC or until complete dissolution of CTAB and n-decanol. The stock solutions were cooled down to room temperature prior to further use. In a second step, 1-2 nm Au seeds were prepared by adding 200 µL of $HAuCl_4$ (50 mM), followed by 100 µL of ascorbic acid (100 mM), and 200 µL of a freshly prepared $NaBH_4$ solution (20 mM), to 20 mL of a CTAB (50 mM)/ n-decanol (13.5 mM) solution under vigorous stirring at 25 ºC. The resulting brownish-yellow seed solution was aged for 60 minutes at room temperature. Subsequently, small anisotropic seeds (small Au NRs) were synthesized. In a 250 mL Erlenmeyer flask containing 100 mL of CTAB (50 mM)/ n-decanol (13.5 mM) solution, we added sequentially 1 mL of $HAuCl_4$ (50 mM), 800 µL of $AgNO_3$ (100 mM), 7 mL of HCl (1 M), and 1.3 mL of ascorbic acid (100 mM). The temperature of the mixture was maintained at 25 ºC throughout the reaction. To this solution, 6 mL of Au seeds was added under stirring and the resulting mixture was left undisturbed for 4 hours at 25 ºC. The resulting colorless solution changes over time to dark brownish grey, indicating the formation small anisotropic seeds of length 21 $\pm$ 4 nm and width 7 $\pm$ 2 nm, with LSPR at 728 nm. After washing by centrifugation at 14,500 rpm for 45

minutes using 2 mL Eppendorf tubes, the precipitate was redispersed in a CTAB solution (10 mM). The concentration of the final anisotropic seed stock was set at 4.5 mM. In the final overgrowth step, 100 mL of a CTAB (50 mM)/ n-decanol (11 mM) solution was added to a 250 mL Erlenmeyer flask. To the above-mentioned solution, 1 mL of $HAuCl_4$ (50 mM), together with selected amounts of $AgNO_3$ (100 mM), HCl (1 M), and 800 µL of ascorbic acid (100 mM) were added under mild stirring. As the solution turned colorless, selected amounts of anisotropic seeds were introduced to the above mixture, under stirring. The aspect ratio of the as synthesized Au NRs was tuned by varying the amount of $AgNO_3$, HCl, and seed (see **Table 3**). As-synthesized Au NRs were then centrifuged at 5000-8000 rpm (15-20 minutes) and redispersed in 10 mL of an aqueous CTAC solution (5 mM). This step was repeated twice to remove excess CTAB. The concentration was adjusted by dilution with Milli-Q water, prior to Ag overgrowth.

Table 3. Growth conditions for the synthesis of SC Au NR of varying aspect ratios.

LSPR [nm]	Aspect ratio	$AgNO_3$ [mL]	HCl [mL]	Seed [mL]	Length [nm]	Width [nm]	Temperature [˚C]
780	3.7	2	2	2.65	41 ± 4	11 ± 2	28
920	5	1.5	10	1.0	66 ± 5	13 ± 2	28

Synthesis of pentatwinned Au nanorods (PT Au NRs):[52] Pentatwinned gold NPs (NRs and BPs) were prepared an initial step comprising a mild thermal treatment of standard seeds (~1.5 nm). A freshly prepared $NaBH_4$ solution (0.025 M, 0.25 mL) was mixed with an aqueous solution composed of $HAuCl_4$ (2.5 mL, 1 mM), citric acid (2.5 mL, 0.02 M) and CTAC (5 mL, 0.1 M) under vigorous stirring. The resulting seed solution was aged in a water bath at 80 °C for 90 min under mild stirring. For PT Au NR growth, $HAuCl_4$ (0.25 mL, 50 mM) was added to an aqueous growth solution of CTAB (100 mL, 8 mM), and after complexation the mixture

was stirred and cooled down to 20 ºC in a thermostatic bath. After 15 minutes, a solution of AA (0.25 mL, 100 mM) was added to the mixture, and the resulting solution was shaken manually until it turned colorless. Subsequently, a certain volume of as-prepared seed solution (0.6 mL) was added to the growth solution under vigorous shaking and left undisturbed overnight at 20 ºC. PT AuNRs were centrifuged twice in CTAC (10 mM), and finally redispersed in CTAC (10 mM), to a final gold concentration 0.25 mM. The final dimensions of PT AuNRs were 55 ± 2 nm and 11 ± 1 nm.

Synthesis of penta-twinned Au bipyramids (PT Au BPs):[52] The as-prepared thermally treated seed solution (0.5 mL) was injected into an aqueous growth solution containing CTAB (10 mL, 0.1 M), $HAuCl_4$ (0.5 mL, 0.01 M), $AgNO_3$ (0.1 mL, 0.01 M), HCl (0.2 mL, 1 M) and AA (0.08 mL, 0.1 M), under vigorous stirring. The reaction solution was kept in a water bath at 30 °C for 4 h under stirring. As-prepared PT Au BPs were centrifuged at 9000 rpm for 20 min and the precipitate was redispersed in CTAC (1 mL, 0.01 M). Concentrated PT Au BPs were washed once more under the same conditions and stored in the fridge for further use.

Synthesis of Au@Ag core-shell nanoparticles:[53] An appropriate amount of Au NP solution was redispersed in BDAC (10 mM) or CTAC (0.01–0.08 M) and mixed with the selected amount of $AgNO_3$ (0.01 M) and AA (0.1 M), see **Table 4** for details. The mixture was maintained in a water bath at 60 °C for 2 h under stirring, during which Ag was reduced on the Au cores to form Au@Ag core-shell NPs.

Table 4. Growth conditions for Au@Ag core-shell NPs.

Sample ID	Au cores	BDAC or CTAC sol.		Vol. 0.01 M $AgNO_3$ sol. [mL]	Vol. 0.1 M AA sol. (µL)	$[Au^0]/[Ag^{+1}]$
		conc. [M]	vol. [mL]			
NC1	SC-OCTs	0.01	10	0.75	300	0.3
NC2	SC-SPs	0.01	10	0.75	300	0.3

NR1	SC-NRs	0.08	1.0	0.12	60	0.8
NR2	SC-NRs	0.08	1.0	0.12	60	0.8
NR3	PT-NRs	0.01	10	0.25	100	1.0
NR4	PT-BPs	0.01	1.0	0.12	60	0.8

Mesoporous silica coating:[54] Au@Ag core-shell NPs were washed through centrifugation and redispersed in a CTAB solution (2 mM, 5 mL), followed by addition of NaOH (0.1 M, 0.05 mL) and TEOS (20 wt% in ethanol, 0.02 mL). The mixture was kept in a water bath at 45 °C for 2 h. This procedure was repeated for the formation of thicker silica shells. Finally, Au@Ag@SiO_2 NPs were centrifuged several times to remove excess reagents and redispersed in ethanol.

Heating, tomographic series acquisition, and reconstruction: All experiments were performed using a "cubed" Thermo Fisher Scientific Themis Z electron microscope operated at 300 kV in HAADF-STEM mode using a DENSsolutions tomography heating holder with MEMS-based heating chips. Tilt series were acquired over ±70° with tilt increments of 2° using a fast tomography approach, described elsewhere.[37] The reconstruction of the tilt series was performed using the Astra Toolbox 1.8 for MATLAB 2018a.[55] Visualization of the 3D reconstructions was performed using the Amira 5.4.0 software.

Quantification and modeling of alloying degree: Characterization of the 3D elemental distribution, the quantification of the degree of alloying and 3D simulations of alloying dynamics are described in detail in our previous work.[23] In short, we used a quantitative analysis of intensities in HAADF-STEM reconstructions to characterize the 3D elemental distribution and degree of alloying. Diffusion simulations based on the homogeneous isotropic Fick's law (equation 1) were performed for various diffusion coefficients, using the measured 3D elemental distribution before heating as the input structure:

$$\frac{dC}{dt} = D\Delta C \quad (1)$$

where $C = C(x, y, z, t)$ is 3D elemental distribution evolving in time, D is the diffusion coefficient, Δ is the Laplace operator.

Together with the missing wedge artifact, other experimental and data processing factors were taken into account: e.g. minor imperfections in focusing and particle stability during fast tomography acquisition and imperfection of projections alignment during reconstruction. Careful selection of the experimental conditions during data acquisition and processing significantly reduce, but do not eliminate these phenomena completely. The remaining effects may lead e.g. to blurring of NP surfaces, which could be misinterpreted as a thin Ag surface layer. For the diffusion simulations, this artifact was accounted for by applying Gaussian blurring to the simulated data, imitating apparent imperfections in experimental data We additionally incorporated the effect of Poisson noise on the spread of intensities in the simulations and implemented an automated fitting procedure to more accurately retrieve the value for the diffusion coefficient from experimental data. The amount of noise in the experimental reconstructions was estimated using the reconstructions of the particles in the fully alloyed state. To exclude the influence of artifacts coming from the limited tilt range of the sample holder, we used a central slice through the reconstruction in the direction perpendicular to the "missing wedge" of projections. Since the elemental distribution in this case is expected to be completely homogeneous, the remaining intensity variations in the reconstruction can be attributed purely to noise. The scale of noise was estimated by calculating the standard deviation of intensities within the particle mask. Fitting of the simulated alloying curve to experimental metrics was performed by numerical minimization of the mean squared difference between the experimental and simulated data as a function of diffusion coefficient using Brent's algorithm[56] implemented in MATLAB. The uncertainty of the diffusion coefficient fitting was calculated using the finite-difference approximation of Fisher

information at the optimal point of the fitting. Simulations of fully alloyed particles were performed to correct experimental alloying metrics and, in turn, to obtain more accurate values of the diffusion coefficients, compared to fitting the simulated alloying curve to non-corrected experimental metrics (**Figure S8**, Supporting Information).

Supporting Information

Supporting Information is available from the Wiley Online Library or from the author.

Acknowledgements

The funding for this project was provided by European Research Council (ERC Consolidator Grant 815128, REALNANO) and European Commission (grant 731019, EUSMI and grant 26019, ESTEEM). This work was performed under the Maria de Maeztu Units of Excellence Programme–Grant No. MDM-2017-0720, Ministry of Science and Innovation.

Conflict of Interests

The authors declare no conflict of interest.

References:

[1] M. Pelton, J. Aizpurua, G. Bryant, *Laser Photonics Rev.* **2008**, *2*, 136.

[2] E. Petryayeva, U. J. Krull, *Anal. Chim. Acta* **2011**, *706*, 8.

[3] M. Rycenga, C. M. Cobley, J. Zeng, W. Li, C. H. Moran, Q. Zhang, D. Qin, Y. Xia, *Chem. Rev.* **2011**, *111*, 3669.

[4] M. I. Stockman, K. Kneipp, S. I. Bozhevolnyi, S. Saha, A. Dutta, J. Ndukaife, N. Kinsey, H. Reddy, U. Guler, V. M. Shalaev, A. Boltasseva, B. Gholipour, H. N. S. Krishnamoorthy, K. F. Macdonald, C. Soci, N. I. Zheludev, V. Savinov, R. Singh, P. Groß, C. Lienau, M. Vadai, M. L. Solomon, D. R. Barton, M. Lawrence, J. A. Dionne, S. V. Boriskina, R. Esteban, J. Aizpurua, X. Zhang, S. Yang, D. Wang, W. Wang, T. W. Odom, N. Accanto, P. M. De Roque, I. M. Hancu, L. Piatkowski, N. F. Van Hulst, M. F. Kling, *J. Opt.* **2018**, *20*, 043001.

[5] G. Baffou, R. Quidant, *Chem. Soc. Rev.* **2014**, *43*, 3898.

[6] W. R. Erwin, H. F. Zarick, E. M. Talbert, R. Bardhan, *Energy Environ. Sci.* **2016**, *9*, 1577.

[7] Y. Choi, T. Kang, L. P. Lee, *Nano Lett.* **2009**, *9*, 85.

[8] J. Reguera, J. Langer, D. Jiménez De Aberasturi, L. M. Liz-Marzán, *Chem. Soc. Rev.* **2017**, *46*, 3866.

[9] J. M. Stern, J. Stanfield, W. Kabbani, J. T. Hsieh, J. A. Cadeddu, *J. Urol.* **2008**, *179*, 748.

[10] R. Liang, J. Xie, J. Li, K. Wang, L. Liu, Y. Gao, M. Hussain, G. Shen, J. Zhu, J. Tao, *Biomaterials* **2017**, *149*, 41.

[11] M. Kim, J. H. Lee, J. M. Nam, *Adv. Sci.* **2019**, *6*, 1900471.

[12] P. Zijlstra, J. W. M. Chon, M. Gu, *Nature* **2009**, *459*, 410.

[13] S. Linic, P. Christopher, D. B. Ingram, *Nat. Mater.* **2011**, *10*, 911.

[14] X. Li, C. Jia, B. Ma, W. Wang, Z. Fang, G. Zhang, X. Guo, *Sci. Rep.* **2015**, *5*, 1.

[15] Y. Wu, P. Jiang, M. Jiang, T. W. Wang, C. F. Guo, S. S. Xie, Z. L. Wang, *Nanotechnology* **2009**, *20*, 305602.

[16] Y. Cao, R. Jin, C. A. Mirkin, *J. Am. Chem. Soc.* **2001**, *123*, 7961.

[17] S. Link, M. A. El-Sayed, *J. Phys. Chem. B* **1999**, *103*, 4212.

[18] J. G. Hinman, A. J. Stork, J. A. Varnell, A. A. Gewirth, C. J. Murphy, *Faraday Discuss.* **2016**, *191*, 9.

[19] C. M. Gonzalez, Y. Liu, J. C. Scaiano, *J. Phys. Chem. C* **2009**, *113*, 11861.

[20] L. Lu, G. Burkey, I. Halaciuga, D. V. Goia, *J. Colloid Interface Sci.* **2013**, *392*, 90.

[21] M. A. Uppal, M. B. Ewing, I. P. Parkin, *Eur. J. Inorg. Chem.* **2011**, 4534.

[22] J. E. S. Van Der Hoeven, T. A. J. Welling, T. A. G. Silva, J. E. Van Den Reijen, C. La Fontaine, X. Carrier, C. Louis, A. Van Blaaderen, P. E. De Jongh, *ACS Nano* **2018**, *12*, 8467.

[23] A. Skorikov, W. Albrecht, E. Bladt, X. Xie, J. E. S. Van Der Hoeven, A. Van Blaaderen, S. Van Aert, S. Bals, *ACS Nano* **2019**, *13*, 13421.

[24] E. González, J. Arbiol, V. F. Puntes, *Science* **2011**, *334*, 1377.

[25] S. W. Chee, Z. M. Wong, Z. Baraissov, S. F. Tan, T. L. Tan, U. Mirsaidov, *Nat. Commun.* **2019**, *10*, 2831.

[26] T. Shibata, B. A. Bunker, Z. Zhang, D. Meisel, C. F. Vardeman, J. D. Gezelter, *J. Am. Chem. Soc.* **2002**, *124*, 11989.

[27] M. Vara, L. T. Roling, X. Wang, A. O. Elnabawy, Z. D. Hood, M. Chi, M. Mavrikakis, Y. Xia, *ACS Nano* **2017**, *11*, 4571.

[28] R. Huang, Y. H. Wen, G. F. Shao, Z. Z. Zhu, S. G. Sun, *RSC Adv.* **2014**, *4*, 7528.

[29] J. Huang, Y. Yan, X. Li, X. Qiao, X. Wu, J. Li, R. Shen, D. Yang, H. Zhang, *Nano Res.* **2020**, *13*, 2641.

[30] W. Albrecht, J. E. S. van der Hoeven, T.-S. Deng, P. E. de Jongh, A. van Blaaderen, *Nanoscale* **2017**, *9*, 2845.

[31] G. González-Rubio, P. Díaz-Núñez, A. Rivera, A. Prada, G. Tardajos, J. González-Izquierdo, L. Bañares, P. Llombart, L. G. Macdowell, M. A. Palafox, L. M. Liz-Marzán, O. Peña-Rodríguez, A. Guerrero-Martínez, *Science* **2017**, *358*, 640.

[32] P. C. Chen, G. Liu, Y. Zhou, K. A. Brown, N. Chernyak, J. L. Hedrick, S. He, Z. Xie, Q. Y. Lin, V. P. Dravid, S. A. O'Neill-Slawecki, C. A. Mirkin, *J. Am. Chem. Soc.* **2015**, *137*, 9167.

[33] Y. Ni, C. Kan, L. He, X. Zhu, M. Jiang, D. Shi, *Photonics Res.* **2019**, *7*, 558.

[34] X. Wang, C. Kan, J. Xu, X. Zhu, M. Jiang, Y. Ni, *J. Phys. D. Appl. Phys.* **2020**, *53*, 295303.

[35] Y. Bai, C. Gao, Y. Yin, *Nanoscale* **2017**, *9*, 14875.

[36] M. Lasserus, M. Schnedlitz, D. Knez, R. Messner, A. Schiffmann, F. Lackner, A. W. Hauser, F. Hofer, W. E. Ernst, *Nanoscale* **2018**, *10*, 2017.

[37] H. Vanrompay, E. Bladt, W. Albrecht, A. Béché, M. Zakhozheva, A. Sánchez-Iglesias, L. M. Liz-Marzán, S. Bals, *Nanoscale* **2018**, *10*, 22792.

[38] W. Albrecht, E. Bladt, H. Vanrompay, J. D. Smith, S. E. Skrabalak, S. Bals, *ACS Nano* **2019**, *13*, 6522.

[39] W. Albrecht, A. van de Glind, H. Yoshida, Y. Isozaki, A. Imhof, A. van Blaaderen, P. E. de Jongh, K. P. de Jong, J. Zečević, S. Takeda, *Ultramicroscopy* **2018**, *193*, 97.

[40] A. I. Frenkel, *Chem. Soc. Rev.* **2012**, *41*, 8163.

[41] H. Petrova, J. P. Juste, I. Pastoriza-Santos, G. V. Hartland, L. M. Liz-Marzán, P. Mulvaney, *Phys. Chem. Chem. Phys.* **2006**, *8*, 814.

[42] M. Chi, C. Wang, Y. Lei, G. Wang, D. Li, K. L. More, A. Lupini, L. F. Allard, N. M. Markovic, V. R. Stamenkovic, *Nat. Commun.* **2015**, *6*, 8925.

[43] W. Albrecht, T. S. Deng, B. Goris, M. A. Van Huis, S. Bals, A. Van Blaaderen, *Nano Lett.* **2016**, *16*, 1818.

[44] S. Gómez-Graña, B. Goris, T. Altantzis, C. Fernández-López, E. Carbó-Argibay, A. Guerrero-Martínez, N. Almora-Barrios, N. López, I. Pastoriza-Santos, J. Pérez-Juste, S. Bals, G. Van Tendeloo, L. M. Liz-Marzán, *J. Phys. Chem. Lett.* **2013**, *4*, 2209.

[45] Z. Erdélyi, D. L. Beke, *J. Mater. Sci.* **2011**, *46*, 6465.

[46] S. L. M. Mallard W.C., Gardner A.B., Bass R.F., *Phys. Rev.* **1963**, *129*, 617.

[47] M. A. Noah, D. Flötotto, Z. Wang, M. Reiner, C. Hugenschmidt, E. J. Mittemeijer, *Acta Mater.* **2016**, *107*, 133.

[48] Z. Erdélyi, *PhD thesis*, Universite De Droit **2001**.

[49] Y. Khalavka, C. Ohm, L. Sun, F. Banhart, C. Sönnichsen, *J. Phys. Chem. C* **2007**, *111*, 12886.

[50] A. Sánchez-Iglesias, M. Grzelczak, T. Altantzis, B. Goris, J. Pérez-Juste, S. Bals, G. Van Tendeloo, S. H. Donaldson, B. F. Chmelka, J. N. Israelachvili, L. M. Liz-Marzán, *ACS Nano* **2012**, *6*, 11059.

[51] G. González-Rubio, V. Kumar, P. Llombart, P. Díaz-Núñez, E. Bladt, T. Altantzis, S. Bals, O. Peña-Rodríguez, E. G. Noya, L. G. Macdowell, A. Guerrero-Martínez, L. M. Liz-Marzán, *ACS Nano* **2019**, *13*, 4424.

[52] A. Sánchez-Iglesias, N. Winckelmans, T. Altantzis, S. Bals, M. Grzelczak, L. M. Liz-marzán, *J. Am. Chem. Soc.* **2017,** *139*, 107.

[53] X. Zhuo, X. Zhu, Q. Li, Z. Yang, J. Wang, *ACS Nano* **2015**, *9*, 7523.

[54] I. Gorelikov, N. Matsuura, *Nano Lett.* **2008**, *8*, 369.

[55] W. van Aarle, W. J. Palenstijn, J. De Beenhouwer, T. Altantzis, S. Bals, K. J. Batenburg, J. Sijbers, *Ultramicroscopy* **2015**, *157*, 35.

[56] R. P. Brent, *Algorithms for Minimization without Derivatives*, Prentice-Hall,

Englewood Cliffs, NJ, 1973.

Table of Contents

The Influence of Size, Shape, and Twin Boundaries on Heat-induced Alloying in Individual Au@Ag Core-Shell Nanoparticles.

Mikhail Mychinko, Alexander Skorikov, Wiebke Albrecht, Ana Sánchez Iglesias, Xiaolu Zhuo, Vished Kumar, Luis M. Liz-Marzán and Sara Bals**

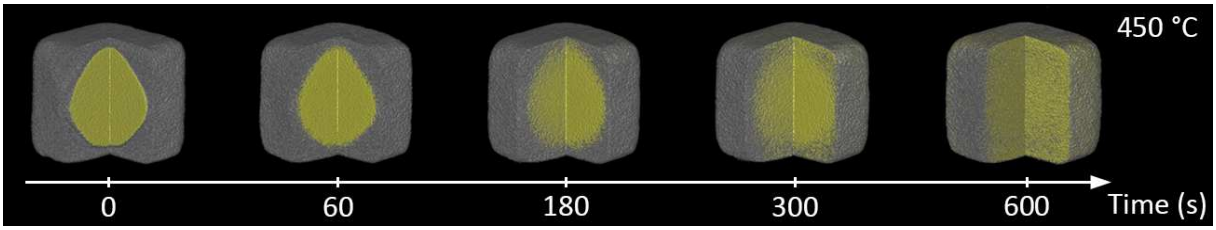

The investigation of heat-induced processes in bimetallic nanoparticles is a key factor for further improvement of their applicability under realistic conditions. We used fast in situ electron tomography to obtain a quantitative characterization of the alloying behavior of various Au@Ag core-shell nanoparticles. In this manner, we were able to disclose the effects deriving from size, aspect ratio, core morphology and the presence of twin boundaries.

Supporting Information:

The Influence of Size, Shape, and Twin Boundaries on Heat-induced Alloying in Individual Au@Ag Core-Shell Nanoparticles.

Mikhail Mychinko, Alexander Skorikov, Wiebke Albrecht, Ana Sánchez Iglesias, Xiaolu Zhuo, Vished Kumar, Luis M. Liz-Marzán and Sara Bals**

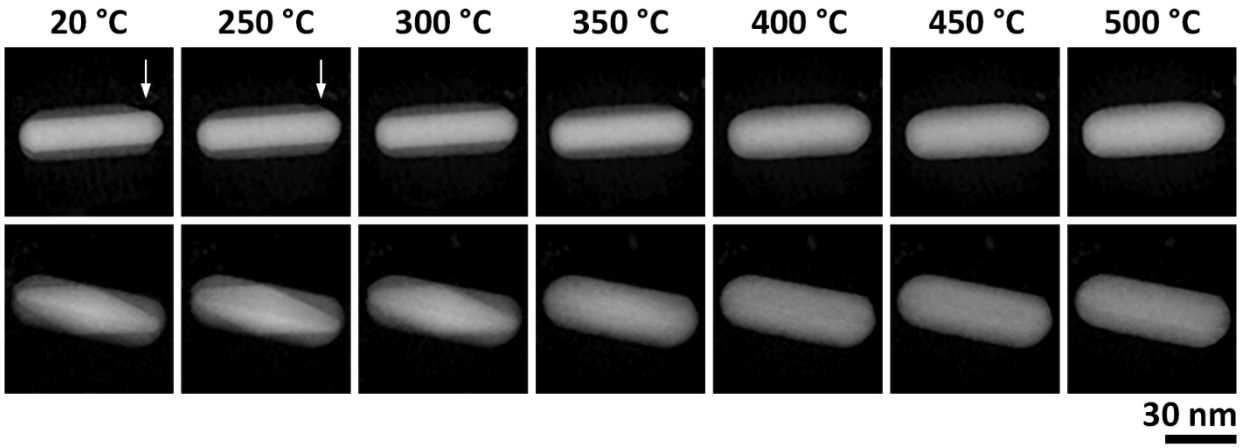

Figure S1. HAADF-STEM images of the atomic redistribution inside an Au@Ag SC-NR (upper row) and an Au PT-NBP@Ag PT-NR (lower row), acquired at room temperature after heating for 5 minutes at the indicated temperature. In this additional experiment, SC-NR and PT-NR with sizes and composition similar to NR2 and NR4 were chosen, which allowed us to estimate 450 °C as an optimal temperature for our alloying experiment.

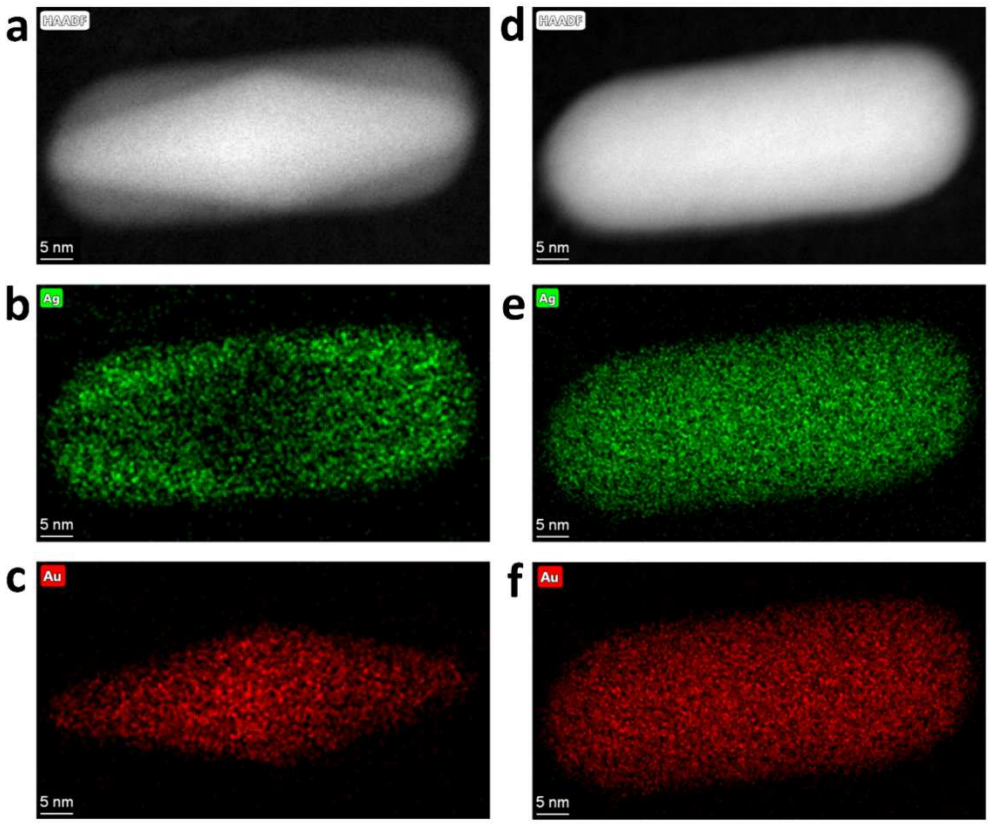

Figure S2. 2D EDX mapping of NR4 before (a-c) and after heating for 600 seconds at 450 °C (d-f).

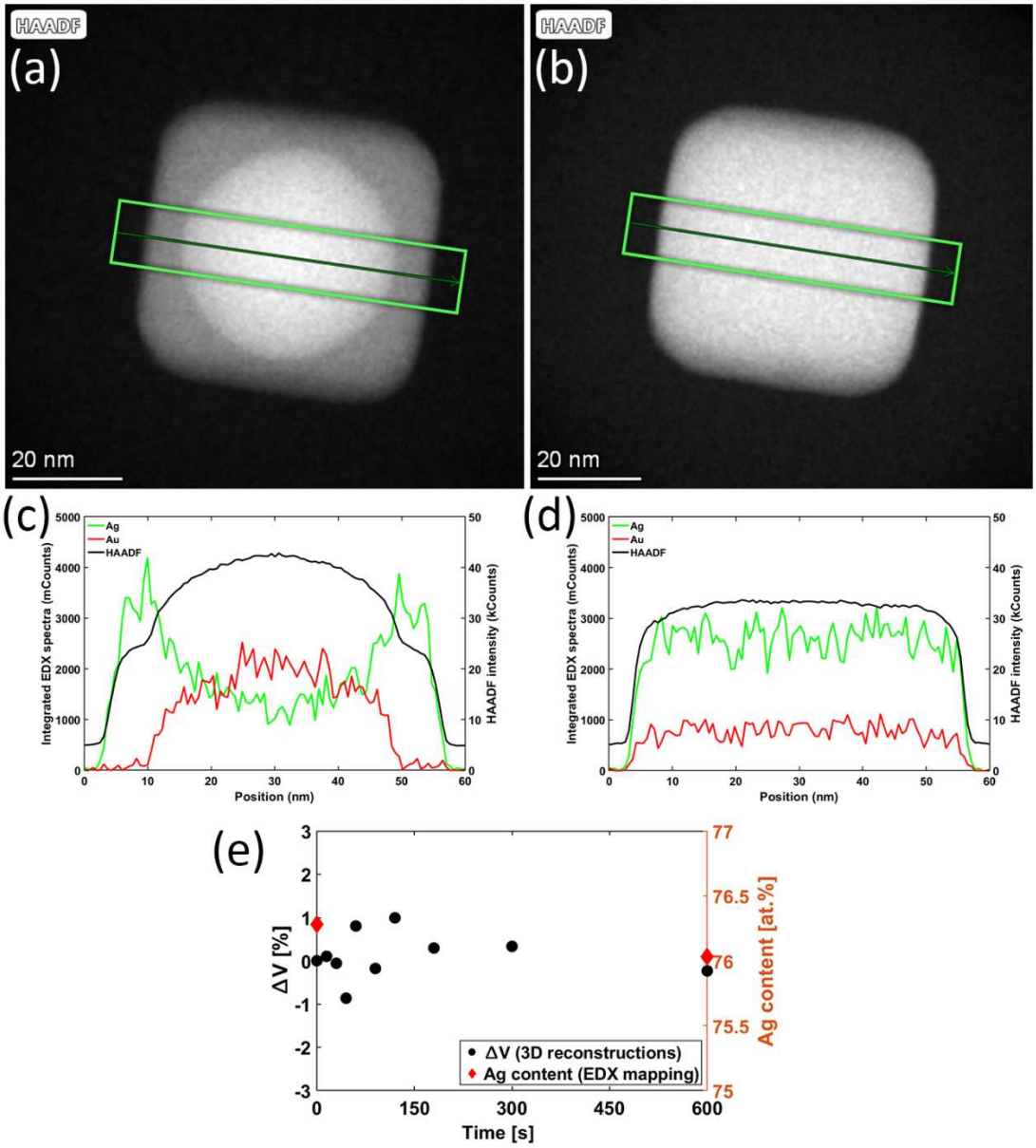

Figure S3. Figure S4. (a,b) HAADF image of NC2 acquired after 0 seconds (a) and 600 seconds (b) of heating. (c,d) Comparison between integrated line profiles based on the same region (green rectangle) of the 2D EDX elemental mapping before (c) and after (d) alloying. (e) Relative volume change (black circles) calculated from 3D reconstructions, and Ag content values (red diamonds) retrieved from EDX mapping before heating (0 s) and after the last heating step (600 s).

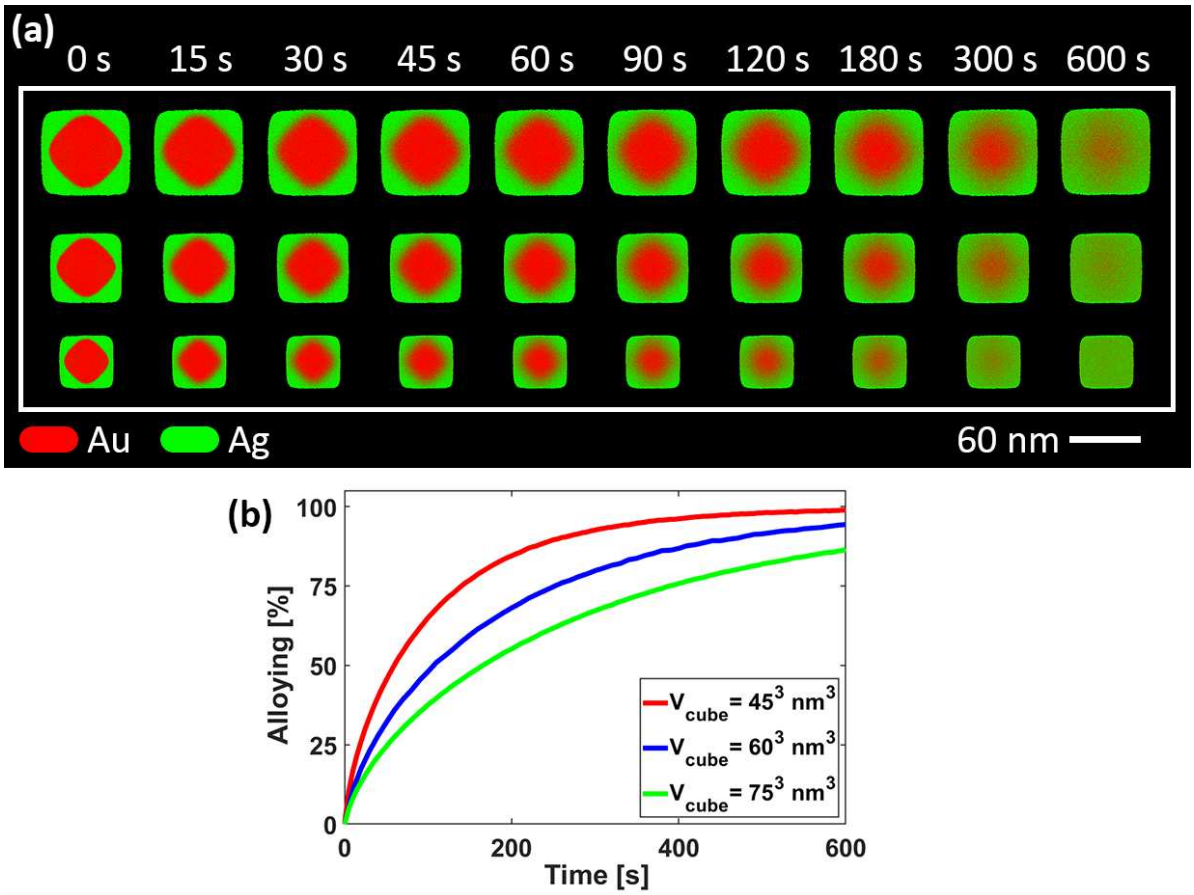

Figure S4. (a) XY-orthoslices through the 3D diffusion simulations for three NCs of similar morphology and composition, but with different sizes: the upper row shows a NC with a 75 nm edge length, the middle row corresponds to a NC with a 60 nm edge length and the lower row shows the evolution of a NC with a 45 nm edge length. The calculated diffusion coefficient for all cases was equal to the value obtained for NC1 (2.7×10^{-19} m^{2}s^{-1}). (b) Comparison of the alloying curves, simulated for three NCs with different size and the same diffusion coefficient: edge lengths are 45 (red curve), 60 (blue curve) and 75 (green curve) nm.

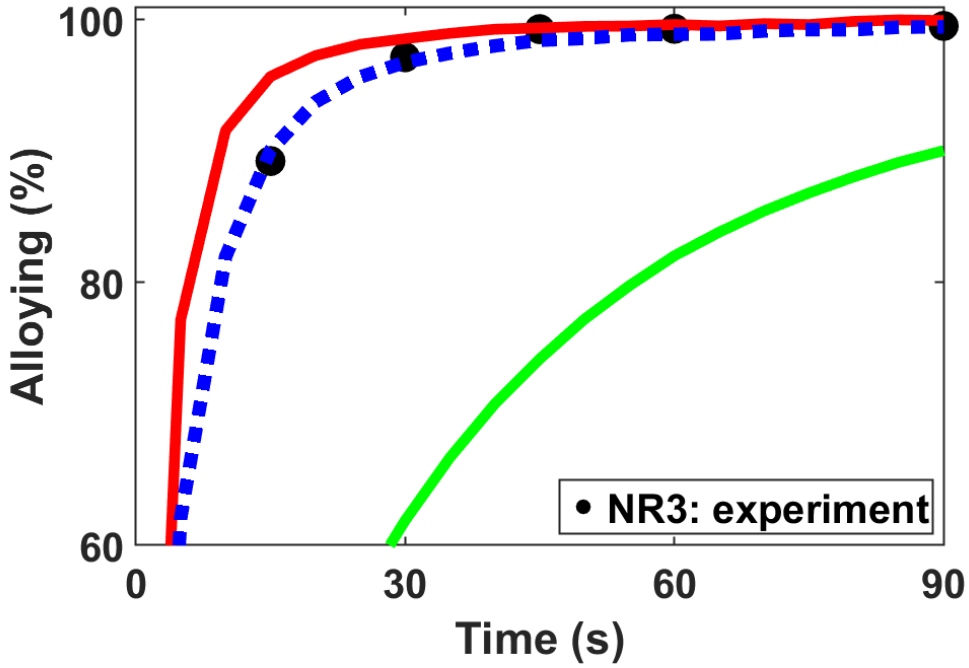

Figure S5. Enlarged fragment of Figure 4d, showing experimental results and diffusion simulations performed for different diffusion coefficients of NR3. The blue dashed curve corresponds to the best fit of simulations to experiments for a diffusion coefficient of 6.3×10^{-19} m^2s^{-1}. The red curve corresponds to simulations based on a diffusion coefficient of 10×10-19 m^2s^{-1}, whereas the green curve was obtained using a diffusion coefficient of 1.0×10^{-19} m^2s^{-1}.

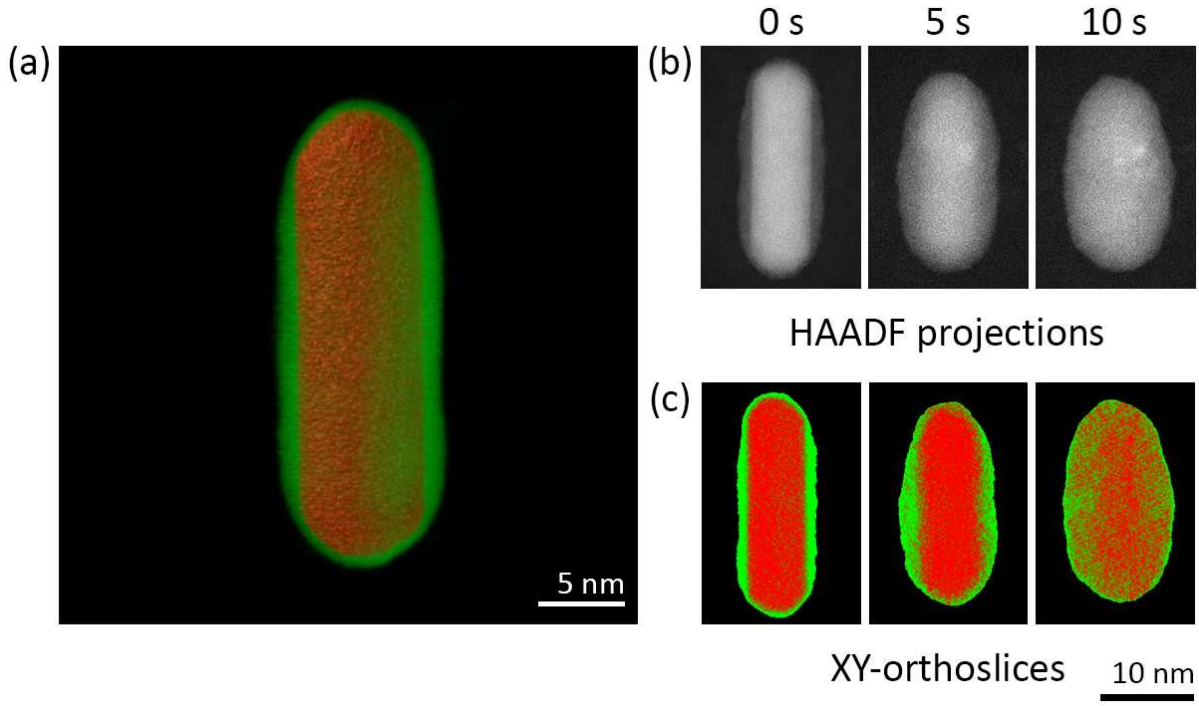

Figure S6. (a) 3D visualization of an Au@Ag small nanorod (SR) with volume ~$1.8*10^3$ nm^3, AR = 2.4, and Au:Ag=56:44; (b) HAADF projections of SR acquired after 0, 5, 10 seconds of heating at 450 °C; (c) YZ-orthoslices through quantified 3D-reconstructions after 0, 5, 10 seconds of heating at 450 °C. The low stability of the particle hinders a quantitative assessment of alloying kinetics.

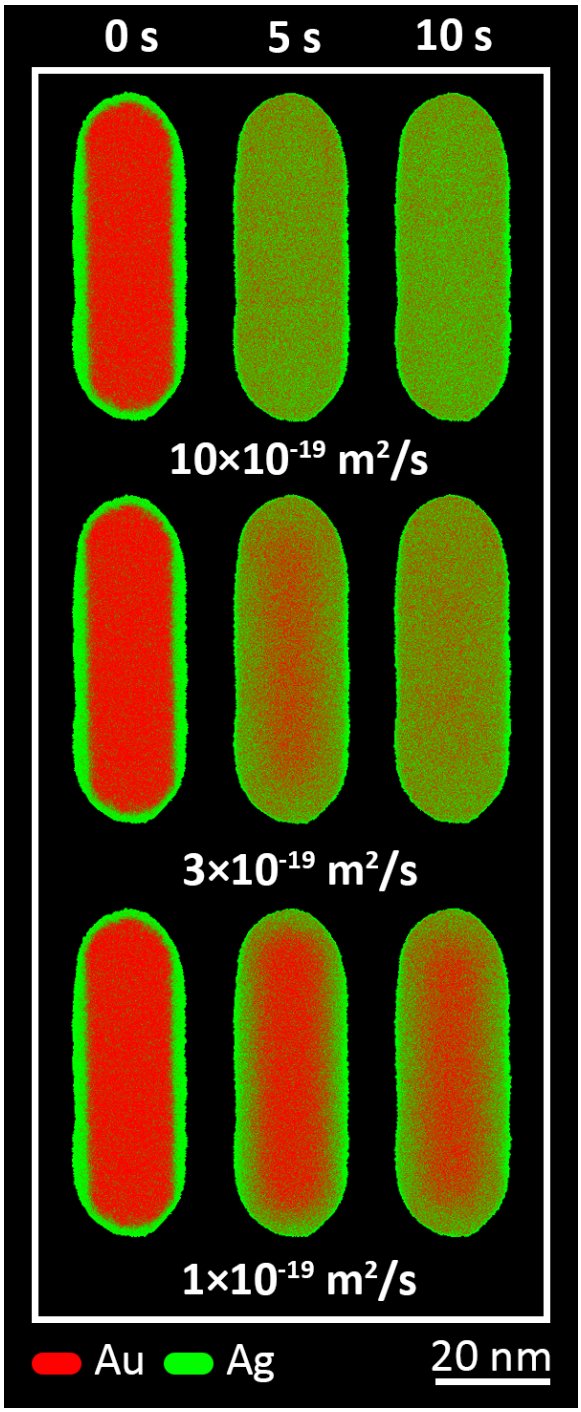

Figure S7. Slices through the 3D diffusion simulations for SR calculated for different values of the diffusion coefficients: 10×10^{-19} m^2/s (upper row), 3×10^{-19} m^2s^{-1} (middle row), 1×10^{-19} m^2s^{-1} (lower row).

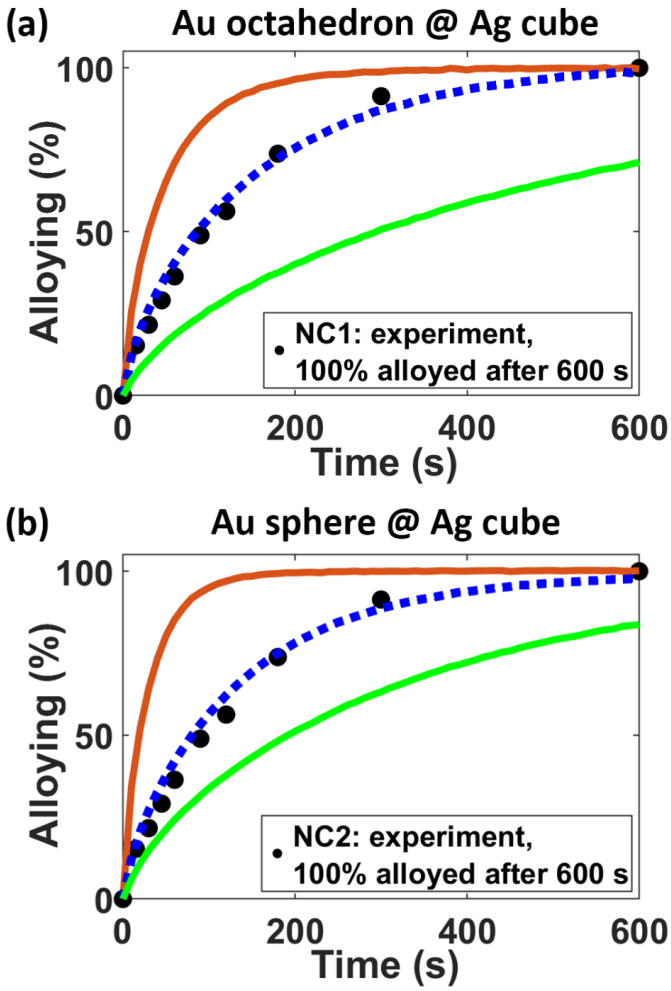

Figure S8. Comparison of the experimental results and diffusion simulations performed for different diffusion coefficients at 450 °C. The black circles indicate the non-corrected degree of alloying (100% after 600 seconds) as quantified from the experimental data (black circles) for NC1 and NC2, respectively. The blue dashed curves correspond to the best fit of simulations to the experiments for diffusion coefficients of 3.3×10^{-19} m^2s^{-1} (a), and 2.7×10^{-19} m^2s^{-1} (b). For both NCs, the red curves correspond to simulations based on a diffusion coefficient value of 10×10^{-19} m^2s^{-1}, whereas the green curves were obtained using a diffusion coefficient value of 1.0×10^{-19} m^2s^{-1}. It is important to note that the values of diffusion coefficients critically depend on the alloying degree after heating.